Magneto-Centrifugal Origin for Protostellar Jets Validated through Detection of Radial Flow at the Jet Base

Chin-Fei Lee^{1,2}, Zhi-Yun Li³, Hsien Shang¹, & Naomi Hirano¹

ABSTRACT

Jets can facilitate the mass accretion onto the protostars in star formation. They are believed to be launched from accretion disks around the protostars by magneto-centrifugal force, as supported by the detections of rotation and magnetic field in some of them. Here we report a radial flow of the textbook-case protostellar jet HH 212 at the base to further support this jet-launching scenario. This radial flow validates a central prediction of the magneto-centrifugal theory of jet formation and collimation, namely, the jet is the densest part of a wide-angle wind that flows radially outward at distances far from the (small, sub-au) launching region. Additional evidence for the radially flowing wide-angle component comes from its ability to reproduce the structure and kinematics of the shells detected around the HH 212 jet. This component, which can transport material from inner to outer disk, could account for the chondrules and Ca-Al-rich inclusions detected in the Solar System at large distances.

Subject headings: accretion, accretion disks — stars: formation — ISM: individual objects (HH 212) — ISM: jets and outflows

1. Introduction

Protostellar jets are seen associated with young stellar objects (Bally 2016; Anglada et al. 2018; Lee 2020). They are ejected from the innermost parts of accretion disks (Ray et al. 2007) and linked to the process of mass accretion onto the central protostars (Cabrit et al.

¹Academia Sinica Institute of Astronomy and Astrophysics, No. 1, Sec. 4, Roosevelt Road, Taipei 10617, Taiwan

² Graduate Institute of Astronomy and Astrophysics, National Taiwan University, No. 1, Sec. 4, Roosevelt Road, Taipei 10617, Taiwan

³Astronomy Department, University of Virginia, Charlottesville, VA 22904, USA

1990; Hartigan et al. 1990). However, how they are launched is still under debate. Recently, they are found to be spinning (Bacciotti et al. 2002; Lee et al. 2017a) and magnetized (Lee et al. 2018a), as expected from magneto-centrifugal launching models, carrying angular momentum away from the disks. However, more observations of protostellar jets are still needed to confirm and constrain the launching models.

HH 212 is a textbook-case protostellar jet because of its well-defined structure with high collimation and symmetry (Zinnecker et al. 1998). The jet is ejected from a rotating accretion disk around a low-mass protostar (Codella et al. 2014; Lee et al. 2017b) at a distance of \sim 400 pc in Orion. It lies almost in the plane of the sky (Claussen et al. 1998). It was recently found to be rotating, carrying angular momentum away from the innermost part of the disk (Lee et al. 2017a), consistent with the magneto-centrifugal launching models. Here, we search for another tell-tale sign to support the models – a radial flow at the base of the jet. This radial flow is required because, in the classic magneto-centrifugal picture (Blandford & Payne 1982), the initially rigid magnetic field lines must be inclined away from the disk normal (i.e., the jet axis) direction by more than 30° in order to centrifugally launch the outflow from the disk surface and accelerate it to a high speed. This requirement means that the magneto-centrifugally driven outflow must start out as a wide-angle wind with a range of flow directions (Shu et al. 1994; Ferreira 1997; Krasnopolsky et al. 2003). As the wind propagates to large distances, inner streamlines are gradually collimated by the "hoop stresses" associated with the toroidal magnetic field into a high-density jet along the axis, while the remaining part remains wide-angled (Shu et al. 1995, Shu1995 hereafter; Krasnopolsky et al. 2003). The slow collimation leads to two generic predictions for the magneto-centrifugally driven jets: (1) the jet material near the base moves in a wider range of radial directions (referred to as "radial flow" hereafter) than farther out, and (2) the jet is always surrounded by a (more tenuous) wide-angle wind. Here we report new observations of HH 212 to test these predictions.

2. Observations

Observations of the HH 212 protostellar system were obtained with Atacama Large Millimeter/submillimeter Array (ALMA) in Band 7 centered at a frequency of ~ 341.5 GHz on 2017 November 27 in Cycle 5 (2017.1.00044.S). The target was observed with a total time of ~ 98 minutes and projected baselines of $\sim 60-8500$ m. Four spectral windows were used, with three in continuum mode having a bandwidth of 2 GHz and one in spectral mode having a bandwidth of 1.875 GHz. The SiO line was included in the spectral mode with a velocity resolution of ~ 1.69 km s⁻¹ per channel. CASA version 5.1 was used to calibrate the

visibility data and generate the SiO line data with continuum subtracted. We used a robust factor of 0.5 for the visibility weighting to generate SiO channel maps with a synthesized beam of 0".036×0".032 (or 14.4 au×12.8 au) at a position angle of $\sim -78^{\circ}$ and a noise level of ~ 0.75 mJy beam⁻¹ (or ~ 7 K) in each channel. These channel maps are then used to generate the total intensity map and position-velocity diagrams.

3. Results

3.1. SiO Observations of the HH 212 Jet

Figure 1 shows the inner part of this jet within 1400 au of the protostar in SiO J=8-7 line. The jet is well detected in SiO within ~ 200 au of the protostar, surrounded by the SO shells (blue dotted curves) detected before (Lee et al. 2021b). It is highly collimated and appears cylindrical (though knotty), extending out from the disk. No SiO jet emission can be seen down to the protostar because it is blocked by the optically thick disk (Lee et al. 2017c). In the south further away, some faint clumpy emission is also seen along the jet axis, tracing the jet itself. In the north further away, a chain of roughly equally spaced wide and flat structures are seen along the jet axis, each one oriented almost perpendicular to the jet axis, probably tracing the internal shocks. Position-velocity (PV) diagram of the SiO emission along the jet axis shows that the radial velocity range (i.e., line width) of the collimated jet along the line of sight (LOS) increases toward the protostar, with its Gaussian FWHM line width increasing from 5–7 km s⁻¹ at 160 au to 16–20 km s⁻¹ at 20 au. It indicates that, despite the cylindrical appearance of the observed jet, the outflowing material in the jet at the base is moving more radially outward from the innermost part of the disk, consistent with magneto-centrifugal models (see e.g., Figure 1d).

A similar increase of line width towards the source has been detected towards more evolved T Tauri jets, e.g., DG Tau and RW Aur (Pyo et al. 2003, 2006). In those cases, the line profiles become more complex towards the sources, showing prominent low-velocity emission referred to as the low-velocity component (LVC). This LVC also shows a decrease in radial velocity towards the source, e.g., in DG Tau (Pyo et al. 2003; Maurri et al. 2014). The observed line width of the RW Aur jet near the source was first found to be too large to be fully explained by a divergent constant velocity flow of 4° in opening angle (Hartigan & Hillenbrand 2009), but later reproduced with an X-wind (Liu & Shang 2012). It is thus not yet clear whether part or all of the LVC traces the wide-angle base of the collimated jet or whether it traces different flow components, e.g., an outer disk wind (Simon et al. 2016; Nisini et al. 2018) or entrained matter.

In the case of HH 212, no clear LVC can be identified in the PV structure. Although the peak emission of knots N1 and N2 shows a decrease of radial velocity towards the source, the line wing emission of these knots extends to higher and lower radial velocities, producing broader line profiles towards the source. The jet interaction with the SO shell at the base could contribute to the widening of the line profiles close to the source on the low-velocity side, since the SO shell has a low velocity near the base (see Section 3.4).

3.2. Velocity and Long-range Acceleration of the HH 212 Jet

Measurements of jet velocity can provide an additional constraint to the models. Figure 2 shows the jet velocity at a distance from ~ 40 to 160,000 au, derived from the proper motion of the SiO jet measured here from ~ 100 to 1000 au (see Appendix) and those previously reported at other distances along the jet axis (Claussen et al. 1998; Lee et al. 2015; Reipurth et al. 2019). Panel a shows the velocities at the measured positions while panel b shows the velocities at the expected positions at the date of current observations assuming ballistic motion. In either case, an apparent acceleration is seen over a large distance, with the velocity increasing from $\sim 50-60~\rm km~s^{-1}$ at 40-50 au, to $\sim 90~\rm km~s^{-1}$ at 1000 au, and then to $\sim 140~\rm km~s^{-1}$ at 3,000 au. The velocity further away remains roughly constant. Current MHD ejection model might have difficulty in producing such a long-range acceleration. Most MHD ejection models predict that terminal jet velocities are reached within a distance of $z=100r_0$, where r_0 is the anchoring radius of the streamline in the disk (Jacquemin-Ide et al. 2019; Tabone et al. 2020). Therefore, further work is needed to check if other effects such as time variability in the ejection velocity and geometrical projection can produce this apparent acceleration.

3.3. Modeling the HH 212 Jet

As discussed earlier, radial flow is a generic feature of the magneto-centrifugal wind at large distances from the (small) launching region. This asymptotic behavior is not only valid for an X-wind (Shu1995), but also for an inner disk wind (Cabrit et al. 1999; Pudritz et al. 2007), especially if mass loading is concentrated towards the inner disk edge (Krasnopolsky et al. 2003). In the X-wind, the gas speed along all streamlines is roughly similar while in the disk wind, the flow speed decreases as the anchoring radius of the streamline increases. The dense core of these winds appears as a collimated jet. For a jet almost in the plane of the sky, the line profile is expected to widen towards the source to both lower and higher velocities, in both the X-wind and disk wind.

We will focus our comparison to the asymptotic X-wind (Shu1995), for which analytic solutions exist. The wind solution is governed by the magnetic field to mass flux ratio β and the amount of specific angular momentum J carried by the gas and field along the streamlines. It is an asymptotically radial wind, but with the central part collimated by the tension force of the toroidal magnetic field into a dense jet. To be specific, we adopt the X-wind parameters reported in Shu1995, with the mean values averaged over the streamlines $\bar{J} \sim 3.7053$ and $\bar{\beta} \sim 1.1675$. This \bar{J} value is similar to the mean value previously found in young protostellar jets (Lee 2020). It determines the terminal velocity and specific angular momentum of the jet to be $\sim v_{k,x}\sqrt{2\bar{J}-3}$ and $\sim \bar{J}\ l_{k,x}$, respectively, where $v_{k,x}$ and $l_{k,x}$ are the Keplerian rotation velocity and specific angular momentum at the launching point called "the X-point".

This asymptotic X-wind model is self-similar and scaled with the mass of the protostar M_* , the radius of the launching point R_x , and the mass-loss rate of the wind M_w . Since the total mass of the protostar and the disk was estimated to be $\sim 0.25 \pm 0.05~M_{\odot}$ (Lee et al. 2017b) and the disk itself was estimated to have a mean mass of $0.10\pm0.05~M_{\odot}$ (Lee et al. 2017c, 2021a), we have $M_* \sim 0.15 \pm 0.07 \ M_{\odot}$. Then with the adopted \bar{J} and the observed specific angular momentum of $\sim 10\pm 3$ au km s⁻¹ (Lee et al. 2017a), we have $l_{k,x} \sim 2.7\pm 0.8$ au km s⁻¹, and thus $R_x \sim 0.05 \pm 0.02$ au and $v_{k,x} \sim 51.7 \pm 15.9$ km s⁻¹. This model produces a terminal jet velocity of $\sim 109\pm33$ km s⁻¹, similar to the mean velocity of the jet and consistent with the jet velocity measured at large distances within the errorbars (see Figure 2). The mass-loss rate in the jet was previously estimated to be $\sim (1.0 \pm 0.5) \times 10^{-6}$ $M_{\odot} \text{ yr}^{-1}$ at a large distance of $\sim 4000-8000$ au (Lee et al. 2015). Considering that the mass-loss rate in the wide-angle component of the X-wind can still be comparable to that in the jet at that large distance (Shu1995), we assume $M_w \sim (1.5 \pm 0.7) \times 10^{-6} M_{\odot} \text{ yr}^{-1}$. The resulting wind velocity, rotation velocity, and density have been given in Shu1995. The jet is the densest core of the wind, with $\beta \sim 1$ and $J \sim 3.2$ within 1000 au of the protostar (see Figure 1 in Shu1995). Using Equation 4b in Shu1995 with these β and J values, we find that the jet velocity in the model increases slowly from 91 ± 28 to 93 ± 29 km s⁻¹ at a distance from 40 and 1000 au. Although the jet velocity at 1000 au in the model is consistent with our measurement, the jet velocity at 40 to 300 au is about two times the observed values there (see Figure 2). The actual X-wind could have a slightly different acceleration efficiency and detailed numerical calculations (Najita & Shu 1994) are needed to fit the observations more closely.

We can compare the model quantitatively to the observed SiO jet up to a distance of \sim 160 au, where no clear internal shocks are seen affecting the structure and kinematics. Since we do not intend to reproduce the observed knotty structure in the jet, which could be due to episodic ejections, the X-wind is assumed to be steady. For this comparison, we adopt

 $M_* \sim 0.15~M_{\odot},~R_x \sim 0.05$ au, and $\dot{M}_w \sim 1.5 \times 10^{-6}~M_{\odot}~\rm yr^{-1}$, with the resulting number density and velocity shown in Figure 1d. To mimic the observations, we also include a dusty disk (dark gray) to block the innermost jet and shells (light gray) to set the outer boundary of the X-wind in the model. SiO molecules are assumed to have a temperature of 400 K, as in another young SiO jet HH 211 (Hirano et al. 2006). A radiative transfer code (Lee et al. 2021b) adding the SiO line with an assumption of LTE is used to calculate the model SiO maps and then the model PV diagrams. The inclination angles of the jet are required to be 3° and 1.8° to the plane of the sky for the northern and southern components, respectively, to match the observed mean jet velocity there. This difference in the inclination angles is acceptable, because the jet seems to have a bending of 2°±1° (Lee et al. 2007). Also, as discussed earlier, since the observed jet velocity appears to be a half of that in the current model, the inclination angles could be two times as high, and become roughly the same as those found for the shells later. Without understanding the long-range acceleration, we postpone the modeling of the jet with such inclination angles to a future investigation.

In order to match the observed SiO emission intensity in the jet, the SiO abundance is required to be $[SiO/H] \sim 3.3 \times 10^{-6}$, roughly consistent with the molecular synthesis model (Glassgold et al. 1991) for a collimated fast wind similar to the X-wind. In addition, in order to match the observed width and velocity range at the base of the jet, the SiO abundance is set to zero when the number density (in H) drops below 6×10^6 cm⁻³, as marked by the gray curves in Figure 1d. This density could be considered either as the minimum value required to excite the SiO J=8-7 emission (which has a critical density of $\sim 2.5 \times 10^7$ cm⁻³ (Lee et al. 2021b)), or as the minimum value where the SiO molecules have formed. As seen in Figure 3, the model produces a hollow SiO jet and can roughly reproduce the observed width of the SiO jet after convolution to the observed resolution. This model can also reproduce the PV structure along the jet axis (see Figure 3d), with the Gaussian FWHM line width increasing from $\sim 6 \text{ km s}^{-1}$ at 160 au towards the protostar to $\sim 18 \text{ km s}^{-1}$ at 20 au, similar to the observations. Moreover, as shown in Figure 4, this model can also roughly reproduce the transverse velocity gradients of the knots in the jet due to jet rotation previously obtained at higher resolution (Lee et al. 2017a). This match further supports the jet to be launched by magneto-centrifugal force and the jet indeed carries away roughly the same amount of specific angular momentum as in the model.

3.4. Modeling the Shells Around the HH 212 Jet

Faint hollow shells are also seen in SiO in the north and south surrounding the jet axis extending out from 200-300 au to more than 1000 au, as shown in Figure 5. They connect to

those previously seen in SO at the base back to the disk (blue dotted curves), forming lobe structures around the jet axis. The PV diagram of the SiO emission along the jet axis shows a tilted V-shaped PV structure arising from the shell in the south, and an inverted V-shaped PV structure arising from the shell in the north. These V-shaped PV structures and the previously detected parabolic PV structures of the SO shells near the base (Lee et al. 2018b) form tilted lobe-shaped PV structures.

Previously, the shells were thought to be produced by a pure collimated jet through jet-driven bow shocks at the tips of the shells (Lee et al. 2021b). However, the spur PV structures, which are the signatures of the jet-driven bow shocks and have a large velocity range at the bow tips due to sideways ejection (Lee et al. 2001; Tabone et al. 2018), are not seen here in the PV diagram at the tips of the shells. Instead, the shells could be driven by X-winds that have wide-angle radial components, because tilted lobe-shaped PV structures have been modeled before with such winds to account for the large-scale molecular outflows around the jets (Shu et al. 1991; Lee et al. 2001; Shang et al. 2020).

Here we construct a momentum-driven shell model to account for the structure and kinematics of the shells. In this model, the shells are produced as the X-wind expands into the extended disk wind coming out from the outer disk detected before in SO (Tabone et al. 2020; Lee et al. 2021b). This extended disk wind is a hollow wind launched from the outer disk with a radius from ~ 4 to 40 au. It is magnetic and vanishes inside 4 au, probably because of a decrease of disk magnetization (Lee et al. 2021b). It has a mass-loss rate of $\sim 10^{-6} M_{\odot} \text{ yr}^{-1}$, with the number density decreasing with the increasing height from the disk midplane approximately as (in spherical coordinates)

$$n_d \sim 6 \times 10^6 \left(\frac{\sin \theta}{\sin 45^\circ}\right) \left(\frac{100 \text{ au}}{r \cos \theta}\right)^p \text{ cm}^{-3}$$
 (1)

where the power-law index p = 4/3. Here the sine factor is to make the wind hollow, with θ being the angle measured from the jet axis. Since the SO emission derived from this wind decreases with height slower than that detected in the observations (Lee et al. 2021b), the actual density of the wind could decrease faster with height. Therefore, we increase from p = 4/3 to p = 2, which also simplifies our calculation of the shells later. The velocity of the extended disk wind is much smaller than that of the X-wind and thus ignored in our calculation. According to Lee et al. (2001), the resulting shell velocity is

$$v_s = \frac{v_w}{1 + \eta^{-1/2}} \tag{2}$$

where v_w is the velocity of the X-wind and $\eta = n_w/n_d$, with n_w and n_d being the number density of the X-wind and disk wind, respectively. At the tip of the shell, $\eta \gg 1$ and thus

 $v_s \sim v_w$. The resulting shell has a lobe-like structure with

$$r_s \approx \frac{L}{1 + \eta^{-1/2}} \tag{3}$$

where L is length of the lobe.

Figure 5 shows the model structure in red dotted curves and model PV structure in red solid curves, with $v_w \sim 90$ km s⁻¹ and $L \sim 1050$ au in the north and 1350 au in the south, as measured from the observations. The shells have a dynamical age of $\sim L/v_w$, the same as their associated jet component, about ~ 60 yrs. The inclination angle of the shell to the plane of sky is $\sim 6^{\circ}$ in the north and 3° in the south. Like the jet, the small difference of inclination angles between the two sides is acceptable. As can be seen, this model reproduces the shell structure and kinematics reasonably well. Moreover, in this model, the shell velocity increases to ~ 20 -25 km s⁻¹ at a distance of ~ 300 au from the protostar, high enough to sputter Si or SiO from the grains in the dusty disk wind and form the SiO in the gas phase (Schilke et al. 1997), producing the observed SiO emission in the shells.

4. Summary and Discussion

Regardless of the uncertainties in the model parameters and measurements, the simple X-wind model can still reproduce the key features (including radial flow, rotation, and structure) of the jet as the densest core of the wind and the key features (including structure and kinematics) of the shells with the interaction between the wide-angle radial component of the wind and an extended dusty disk wind. It is expected that an inner disk wind can also reproduce the key features. Thus, the jet is likely a dense core of either an X-wind or an inner disk wind.

Interestingly, the wide-angle radial component, if does exist, can also solve other existing problems. In particular, since a pure collimated jet has difficulty in producing the observed width and kinematics of large-scale molecular outflows (Lee et al. 2002), the wide-angle radial component can provide a promising solution to the width and kinematic problems of those outflows (Lee et al. 2000; Shang et al. 2006; Arce et al. 2007; Zhang et al. 2019). Moreover, it is still unclear why chondritic materials and Ca-Al-rich inclusions are detected throughout the Solar System. It could be that they were originally produced during the star formation in the innermost disk where the temperature was high enough to form them, but later flung out by the wide-angle wind component to rain down everywhere in the disk (Shang et al. 2000).

We thank the anonymous referee for insightful comments. This paper makes use of the following ALMA data: ADS/JAO.ALMA#2017.1.00044.S. ALMA is a partnership of ESO (representing its member states), NSF (USA) and NINS (Japan), together with NRC (Canada), NSC and ASIAA (Taiwan), and KASI (Republic of Korea), in cooperation with the Republic of Chile. The Joint ALMA Observatory is operated by ESO, AUI/NRAO and NAOJ. C.-F.L. acknowledges grants from the Ministry of Science and Technology of Taiwan (MoST 107-2119-M-001-040-MY3, 110-2112-M-001-021-MY3) and the Academia Sinica (Investigator Award AS-IA-108-M01). Z.-Y.L. is supported in part by NASA 80NSSC20K0533 and NSF AST-1910106.

REFERENCES

Anglada, G., Rodríguez, L. F., & Carrasco-González, C. 2018, A&A Rev., 26, 3. doi:10.1007/s00159-018-0107-z

Arce, H. G., Shepherd, D., Gueth, F., et al. 2007, Protostars and Planets V, 245

Bacciotti, F., Ray, T. P., Mundt, R., et al. 2002, ApJ, 576, 222. doi:10.1086/341725

Bally, J. Protostellar Outflows. ARA&A,54,491 (2016)

Blandford, R. D. & Payne, D. G. 1982, MNRAS, 199, 883. doi:10.1093/mnras/199.4.883

Cabrit, S., Edwards, S., Strom, S. E., et al. 1990, ApJ, 354, 687. doi:10.1086/168725

Cabrit, S., Ferreira, J., & Raga, A. C. 1999, A&A, 343, L61

Claussen, M. J., Marvel, K. B., Wootten, A., et al. 1998, ApJ, 507, L79. doi:10.1086/311669

Codella, C., Cabrit, S., Gueth, F., et al. 2014, A&A, 568, L5. doi:10.1051/0004-6361/201424103

Ferreira, J. 1997, A&A, 319, 340

Glassgold, A. E., Mamon, G. A., & Huggins, P. J. 1991, ApJ, 373, 254. doi:10.1086/170045

Hartigan, P., Hartmann, L., Kenyon, S. J., et al. 1990, ApJ, 354, L25. doi:10.1086/185714

Hartigan, P. & Hillenbrand, L. 2009, ApJ, 705, 1388. doi:10.1088/0004-637X/705/2/1388

Hirano, N., Liu, S.-Y., Shang, H., et al. 2006, ApJ, 636, L141. doi:10.1086/500201

- Jacquemin-Ide, J., Ferreira, J., & Lesur, G. 2019, MNRAS, 490, 3112. doi:10.1093/mnras/stz2749
- Krasnopolsky, R., Li, Z.-Y., & Blandford, R. D. 2003, ApJ, 595, 631. doi:10.1086/377494
- Lee, C.-F., Mundy, L. G., Reipurth, B., et al. 2000, ApJ, 542, 925. doi:10.1086/317056
- Lee, C.-F., Stone, J. M., Ostriker, E. C., et al. 2001, ApJ, 557, 429. doi:10.1086/321648
- Lee, C.-F., Mundy, L. G., Stone, J. M., et al. 2002, ApJ, 576, 294. doi:10.1086/341540
- Lee, C.-F., Ho, P. T. P., Hirano, N., et al. 2007, ApJ, 659, 499. doi:10.1086/512540
- Lee, C.-F., Hirano, N., Zhang, Q., et al. 2015, ApJ, 805, 186. doi:10.1088/0004-637X/805/2/186
- Lee, C.-F., Ho, P. T. P., Li, Z.-Y., et al. 2017a, Nature Astronomy, 1, 0152. doi:10.1038/s41550-017-0152
- Lee, C.-F., Li, Z.-Y., Ho, P. T. P., et al. 2017b, ApJ, 843, 27. doi:10.3847/1538-4357/aa7757
- Lee, C.-F., Li, Z.-Y., Ho, P. T. P., et al. 2017c, Science Advances, 3, e1602935. doi:10.1126/sciadv.1602935
- Lee, C.-F., Hwang, H.-C., Ching, T.-C., et al. 2018a, Nature Communications, 9, 4636. doi:10.1038/s41467-018-07143-8
- Lee, C.-F., Li, Z.-Y., Codella, C., et al. 2018b, ApJ, 856, 14. doi:10.3847/1538-4357/aaae6d
- Lee, C.-F. 2020, A&A Rev., 28, 1. doi:10.1007/s00159-020-0123-7
- Lee, C.-F., Li, Z.-Y., Yang, H., et al. 2021a, ApJ, 910, 75. doi:10.3847/1538-4357/abe53a
- Lee, C.-F., Tabone, B., Cabrit, S., et al. 2021b, ApJ, 907, L41. doi:10.3847/2041-8213/abda38
- Liu, C.-F. & Shang, H. 2012, ApJ, 761, 94. doi:10.1088/0004-637X/761/2/94
- Maurri, L., Bacciotti, F., Podio, L., et al. 2014, A&A, 565, A110. doi:10.1051/0004-6361/201117510
- Najita, J. R. & Shu, F. H. 1994, ApJ, 429, 808. doi:10.1086/174365
- Nisini, B., Antoniucci, S., Alcalá, J. M., et al. 2018, A&A, 609, A87. doi:10.1051/0004-6361/201730834

- Pudritz, R. E., Ouyed, R., Fendt, C., et al. 2007, Protostars and Planets V, 277
- Pyo, T.-S., Hayashi, M., Kobayashi, N., et al. 2006, ApJ, 649, 836. doi:10.1086/506929
- Pyo, T.-S., Kobayashi, N., Hayashi, M., et al. 2003, ApJ, 590, 340. doi:10.1086/374966
- Ray, T., Dougados, C., Bacciotti, F., et al. 2007, Protostars and Planets V, 231
- Reipurth, B., Davis, C. J., Bally, J., et al. 2019, AJ, 158, 107. doi:10.3847/1538-3881/ab2d25
- Schilke, P., Walmsley, C. M., Pineau des Forets, G., et al. 1997, A&A, 321, 293
- Shang, H., Shu, F. H., Lee, T., et al. 2000, Space Sci. Rev., 92, 153. doi:10.1023/A:1005234909848
- Shang, H., Allen, A., Li, Z.-Y., et al. 2006, ApJ, 649, 845. doi:10.1086/506513
- Shang, H., Krasnopolsky, R., Liu, C.-F., et al. 2020, ApJ, 905, 116. doi:10.3847/1538-4357/abbdb0
- Shu, F. H., Ruden, S. P., Lada, C. J., et al. 1991, ApJ, 370, L31. doi:10.1086/185970
- Shu, F. H., Najita, J., Ostriker, E. C., et al. 1995, ApJ, 455, L155. doi:10.1086/309838
- Shu, F., Najita, J., Ostriker, E., et al. 1994, ApJ, 429, 781. doi:10.1086/174363
- Simon, M. N., Pascucci, I., Edwards, S., et al. 2016, ApJ, 831, 169. doi:10.3847/0004-637X/831/2/169
- Tabone, B., Raga, A., Cabrit, S., et al. 2018, A&A, 614, A119. doi:10.1051/0004-6361/201732031
- Tabone, B., Cabrit, S., Pineau des Forêts, G., et al. 2020, A&A, 640, A82. doi:10.1051/0004-6361/201834377
- Zhang, Y., Arce, H. G., Mardones, D., et al. 2019, ApJ, 883, 1. doi:10.3847/1538-4357/ab3850
- Zinnecker, H., McCaughrean, M. J., & Rayner, J. T. 1998, Nature, 394, 862 doi:10.1038/29716

This preprint was prepared with the AAS IATEX macros v5.2.

A. Proper Motion

Proper motion of the jet can be measured by comparing the SiO total intensity map of the jet presented in this paper to that obtained about 2 years earlier on 2015 November 05 and December 03 reported in Lee et al. (2017a). The SiO map taken earlier has been convolved to have the same angular resolution as that here. As shown in Figure A1, the jet shows roughly the same structures in the two epochs. The white arrows show the position shifts of the isolated knots and internal shocks of the jet between the two epochs. The inner knots are not spatially well resolved, and only knots N2, N4, and S3 can be roughly separated to measure the proper motion (see Figure A1b for the zoomin). The position shifts are found to range from 0″.05 to 0″.11, which is ~ 1.5 to 3 synthesized beams. Due to the cooling, expansion, and other factors, the emission features from the same gas could be different between the two epochs. Hence the uncertainties of the measurements are assumed to be a half of the position shifts. The proper motion can then be obtained by dividing the position shifts by the duration of 2 years.

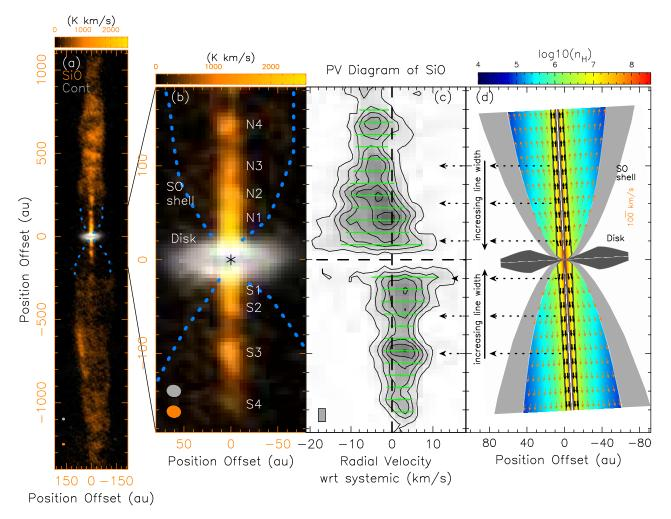


Fig. 1.— The HH 212 jet and model: (a) shows the SiO total intensity map (orange) of the jet within 1400 au of the protostar at 0".036×0".032 resolution integrated from -16.1 to 17.6 km s⁻¹, with the 350 GHz continuum map (gray, adopted from Lee et al. (2021b)) of the dusty disk. They are rotated by 22.5° clockwise to align the jet axis vertically. The dotted blue curves show the shells previously detected in SO (Lee et al. 2021b). (b) shows the innermost jet within \sim 200 au of the protostar, with the nomenclature of the knots from Lee et al. (2017a). (c) shows the PV diagram along the jet axis for the innermost jet, made with a transverse width of 8 au. The contours start at 3σ with a step of 4.5σ , where $\sigma = 5.8$ K. The green lines show the FWHM line widths obtained from Gaussian fit. (d) shows the number density and velocity in our X-wind model, with the dusty disk (dark gray) and shells (light gray), illustrating the increase of SiO line width of the jet towards the protostar. Here the jet is the densest core of the wind outlined by the gray curves.

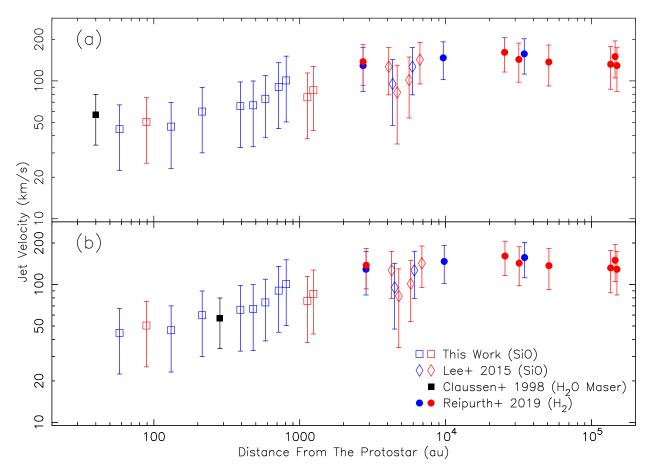


Fig. 2.— Jet velocity of HH 212 measured at a distance from \sim 40 to 160,000 au. They are derived from the proper motion of the SiO jet measured here from \sim 100 to 1000 au (see Appendix) and those previously reported at other distances along the jet axis (Claussen et al. 1998; Lee et al. 2015; Reipurth et al. 2019). Red and blue data points are for the redshifted and blueshifted jet components, respectively. Since the jet is almost in the plane of the sky, the jet velocity is the same as the proper motion. In (b), the data points are shifted to their expected positions at the mean date (2016 Nov) of the new ALMA observations, assuming ballistic motion.

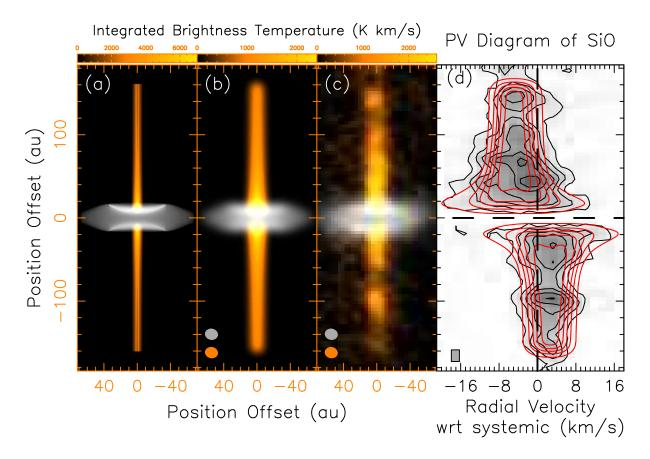


Fig. 3.— Comparison of the X-wind model and the observations of the HH 212 jet. (a) shows the SiO map of the jet and the 350 GHz continuum map of the disk derived from the model. (b) shows the map of the jet and disk convolved to the observed resolution. (c) shows the observed SiO jet and dusty disk. (d) shows the comparison of the PV structures between the model (red contours) and observations (gray image with black contours). Contour levels are the same as those in Figure 1c.

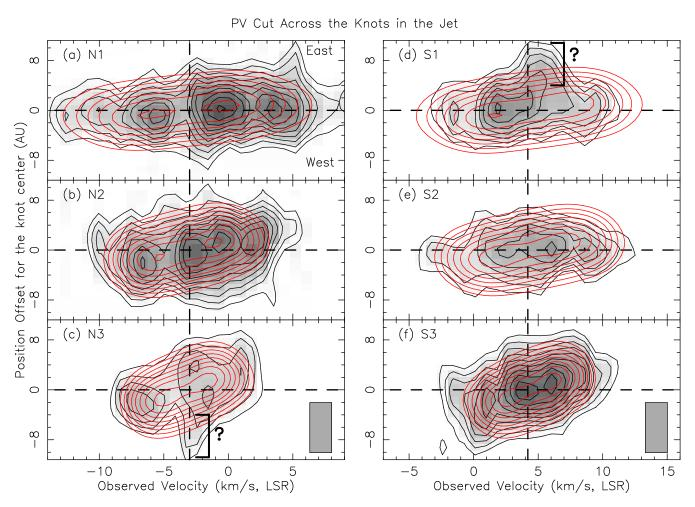


Fig. 4.— Comparison of the velocity gradients in the PV structures across the knots in the innermost jet due to jet rotation. The observed PV structures (black contours with gray image) were adopted from Lee et al. (2017a) at 8 au spatial resolution and 1.7 km s⁻¹ velocity resolution. The model PV structures (red contours) are derived from the X-wind model at the same resolutions. The contour levels start from 4σ with a step of 1σ , where $\sigma = 21.3$ K.

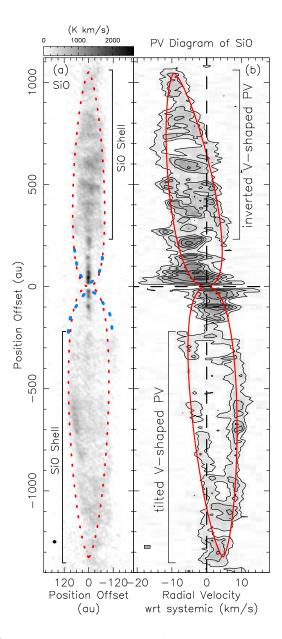


Fig. 5.— Comparison of the shell structure and PV structure along the jet axis between the model and observations. The model structure (red dotted curves) and the model PV structure (red solid curves) of the shells are derived from an interaction of the X-wind with an extended disk wind. The dotted blue curves outline the shells previously detected in SO (Lee et al. 2021b). The contours start at 3σ with a step of 4.5σ , where $\sigma = 5.8$ K.

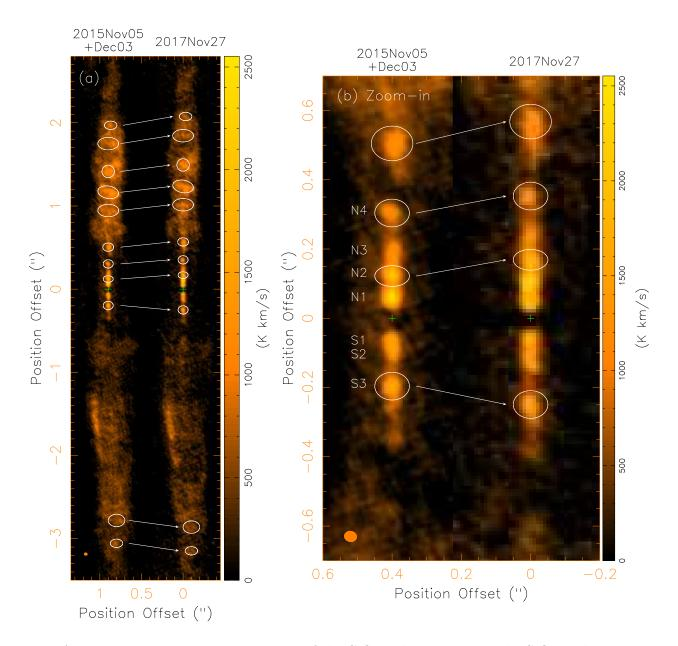


Fig. A1.— Proper motion measurement of the SiO jet by comparing the SiO total intensity maps in two epochs at 0.036×0.032 resolution. The white arrows show the position shifts of the isolated knots and internal shocks (marked with white ellipses) between the two epochs.